Research Article | Vol. 34, No. 1 / 12 Jan 2026 / *Optics Express* 1198

Heterogeneously integrated Vernier laser with 10-nm BCB bonding and their thermal analysis

Sangmin Oh, Jaeseong Jeon, Sushil Tandukar, Juwon Kim, Baekhyeong Lee, Sangeon Park, Wongon Lee, and Il-Sug Chung*

Department of Electrical Engineering Ulsan National Institute of Science and Technology, Ulsan 689-798, Republic of Korea
*ischung@unist.ac.kr

Abstract: We report heterogeneously integrated Si/III-V two-ring Vernier lasers featuring a 10-nm divinylsiloxane-bis-benzocyclobutene (BCB) bonding layer, which is the thinnest to our knowledge. The fabricated laser device demonstrates a double-facet output power of 13.6 mW, a linewidth of 2.6 kHz, a free spectral range (FSR) of 40 nm, and a side mode suppression ratio (SMSR) of 46 dB. These values are comparable to those of a directly bonded Vernier laser structure, which is thermally ideal. The comparability is attributed to a small thermal impedance value of 45.1 K/W, which was experimentally measured with what we believe to be a new method developed for lasers with extensive passive sections. A laser model calibrated with experimental inputs predicts that the output power of a 10-nm BCB bonded Vernier laser with a 4-µm current aperture differs from that of a directly bonded one by less than 10% even beyond a thermal rollover. It is also anticipated that the 10-nm BCB bonded laser can emit a few mW even at an ambient temperature of 120 °C. Such a high-temperature operation capability is desirable for light detection and ranging (LiDAR) chip applications. The investigated 10-nm BCB bonding approach can be an attractive alternative for cases where a relaxed surface roughness condition is beneficial.

© 2026 Optica Publishing Group under the terms of the Optica Open Access Publishing Agreement

1. Introduction

With the rapid advancement of high-speed and highly integrated photonic applications such as co-packaged optics (CPO) [1–3], photonic processors [4–6], LiDAR [7–10], and quantum computing/communications [11–14], the demand for photonic integrated circuits (PICs) has been continuously increasing. Among various building block devices of PICs, integrated lasers are essential, providing performance advantages and design flexibilities. Targeting low energy consumption for communications, integrated photonic crystal lasers [15], integrated ring lasers [16], and integrated vertical cavity lasers [17,18] have been reported. Short-cavity DFB or DR lasers have been reported for more than 100 Gbit/s direct modulation [19,20]. Single-mode DFB lasers with low threshold and moderate output power are adequate for WDM light sources in CPO applications [21], eliminating the need for lossy fiber coupling of external light sources. Narrow-linewidth and tunable lasers based on Vernier rings are promising for long-distance FMCW LiDAR chip applications [16].

Several approaches have been explored to integrate III–V gain materials onto silicon or Si_3N_4, including heterogeneous integration [22–26], hybrid integration [27,28], micro-printing [29] and direct epitaxial growth [30,31]. Though there has been significant advancement in integrated lasers based on group IV materials like Ge or GeSn [32,33], the demonstrated efficiencies at room temperature are not yet comparable to those of III-V materials. In this work, we adopt the heterogeneous integration approach in which III–V gain materials are bonded onto a silicon PIC platform. The heterogeneous integration can be further classified as wafer fusion at high temperatures, for example 600 °C [34,35], direct wafer bonding at low temperatures less than

#582080 https://doi.org/10.1364/OE.582080
Journal © 2026 Received 6 Nov 2025; revised 25 Dec 2025; accepted 25 Dec 2025; published 9 Jan 2026

Optics EXPRESS

300 °C [36–38], and polymer bonding using BCB at 250 to 280 °C [23,24]. Considering the difference in thermal expansion coefficients as well as CMOS fabrication compatibility, direct wafer bonding and BCB bonding are most commonly adopted in the community.

In heterogeneously integrated lasers on the silicon-on-insulator (SOI) platform, heat management is critical for performance such as output power, modulation speed, high ambient temperature operation, aging, noise characteristics, and long-time stability. Heat management includes minimizing the heat generation and efficiently dissipating the generated heat. The former is mostly related to Joule heating, which is quantified by differential resistance, R_d. The latter can be managed by adding an upper-side heat spreader and/or establishing an efficient heat channel toward the bottom side, which is quantified by thermal impedance, Z_T.

With respect to heat dissipation through the bottom side, directly wafer bonded lasers are ideal since there is only a few nanometer-thick native oxide or Al_2O_3 at the bonding interface. Compared to the direct wafer bonding requiring a surface roughness of less than 1 nm for example [39], the BCB-bonded approach relaxes the strict surface flatness requirement. A roughness of less than 20 nm is allowed [40,41], which is beneficial for fabrication ease and yield. From a thermal point of view, however, the poor thermal conductivity of BCB limits effective heat dissipation through the wafer-bonded bottom side. A typical BCB thickness is 100 nm and the minimum thickness so far is 40 nm [23]. The thermal conductivity of BCB is 0.3 W/m K, which is even lower than that of SiO_2, i.e., 1.4 W/m K. Maximum output powers of a directly bonded Fabry-Pérot (FP) laser and a BCB-bonded FP laser reported in the literature are 16 mW and 3 mW, respectively [24,26]. Such a large difference can be attributed to the significant difference in heat dissipation capability.

In this work, we have fabricated heterogeneously integrated dual-ring Vernier lasers, featuring a 10-nm BCB bonding layer and a 4-µm-wide plasma-induced oxide current aperture. The bonding thickness is the thinnest to our knowledge. For experimental estimation of thermal impedances for Vernier laser structures, a correction factor has been introduced, including the significant effect of passive sections on wavelength change. With the revised method, the thermal impedances of the fabricated 10-nm BCB bonded Vernier laser with InAlGaAs/InAlGaAs quantum wells (QWs) and 40-nm BCB bonded reference laser with one ring resonator and InGaAs/InAlGaAs QWs are estimated as 45.1 K/W and 52.3 K/W, which differ from the simulation values by 2.6% and 1.1%, respectively. The revised method works accurately for lasers with different cavity structures and QWs. Without the correction factor, the thermal impedance values are underestimated by a factor of 9. The fabricated 10-nm BCB bonded laser device demonstrates a double-facet output power of 13.6 mW, a linewidth of 2.6 kHz, a free spectral range (FSR) of 40 nm, a side mode suppression ratio (SMSR) of 46 dB, and a threshold current, I_{th} of 130 mA. These performance metrics are comparable to those of a recently-reported directly-bonded Vernier laser except for the threshold current [16]. A laser model is calibrated with experimental inputs of characteristic temperature, T_0, a thermal impedance, Z_T, and L-I-V curves. This laser model estimates the current aperture width, w_a of the fabricated 10-nm BCB bonded laser as 20.2µm, which implies the 10-nm-thick oxide aperture was not effective though this thickness is expected to suppress current tunneling. The calibrated laser model anticipates that a 10-nm BCB bonded laser with a 4-µm current aperture has a threshold current of 24 mA and its output power differs from that of a directly bonded laser by less than 10 % even beyond a thermal roll-over. It also predicts that the 10-nm BCB bonded laser can emit several milliwatts at an ambient temperature of 120 °C, which is required for LiDAR chips being installed in automobiles.

This paper is organized as follows. Section 2 describes device structures and 10-nm BCB related designs. In Section 3, the revised experimental method of estimating thermal impedance is explained. In Section 4, fabrication and characterization results are presented, being followed by thermal analysis and discussions. Then, conclusions and prospects are discussed n Section 5.

Optics EXPRESS

2. Device design

2.1. Device structures

In this work, a two-ring Vernier laser (hereafter, "Vernier laser"), a two-ring Vernier cavity without a III-V section (hereafter, "passive Vernier cavity"), and a one-ring laser (hereafter, "reference laser") structures have been designed, as shown in Figs. 1(a1) to (a3). For comparison, 10-nm and 40-nm BCB bondings are applied to the Vernier laser and reference laser structures, respectively. The passive Vernier cavity is intended for extracting the Q-factor information of rings and pre-estimating the FSR of the Vernier laser cavity.

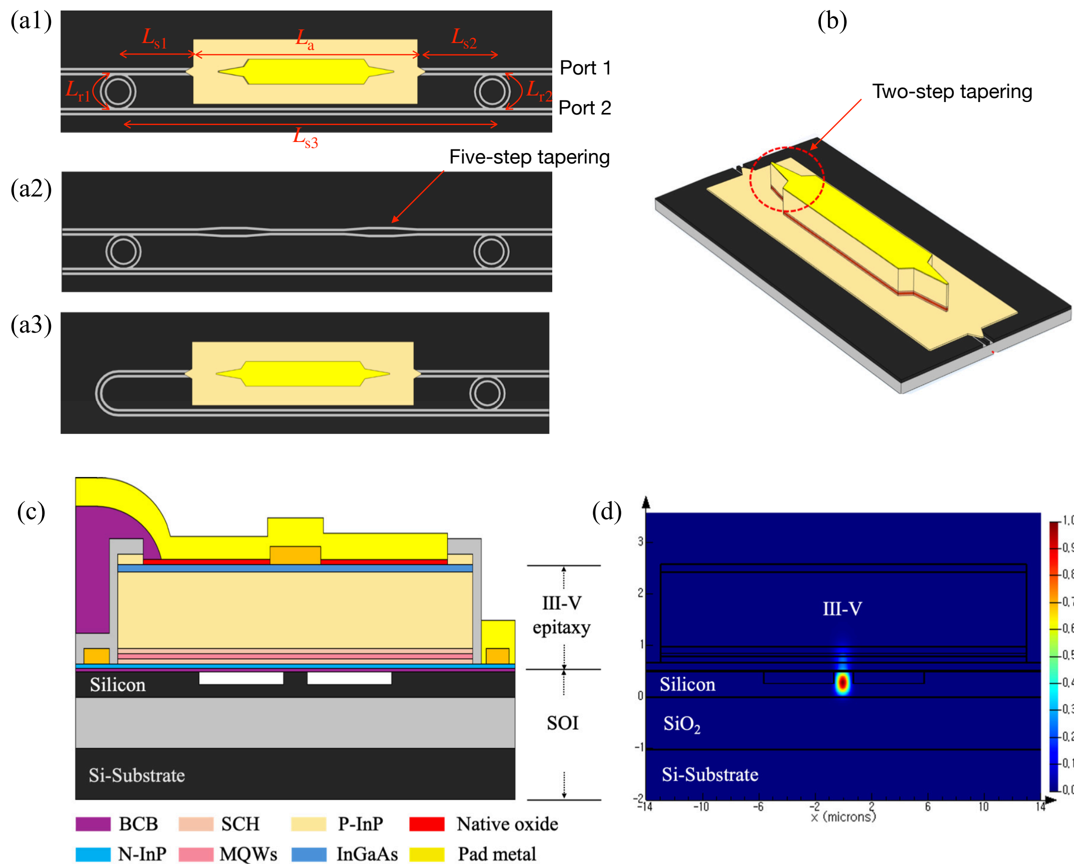

Fig. 1. (a1-a3) Schematic top views of a Vernier laser (a1), a passive Vernier cavity (a2), and an one-ring reference laser (a3). (b) A schematic view of the active section. (c) A schematic cross-section of the active section. (d) A simulated optical mode profile in the active section.

The Vernier laser structure consists of an active section of length L_a and a passive section. The passive section includes straight passive sections of lengths L_{s1}, L_{s2}, and L_{s3}, and two rings of effective lengths L_{r1} and L_{r2}, as shown in Fig. 1(a1). All the length values are listed in Table 1 and the estimation method of effective lengths of rings is explained in Section 3. For maximizing transmission between the passive and active sections, a five-step tapering is applied to the silicon waveguide (see Fig. 1(a2)) while a two-step tapering is adopted for the III-V layers (see Fig. 1(b)). Furthermore, the influence of BCB bonding layer thickness on the transmission is also considered for the laser design (see Figs. 2(b) and (c) and related text). As shown in Fig. 1(c), the III-V layers

Optics EXPRESS

consist of a 110-nm n-InP contact layer, a 125-nm separate-confinement heterostructure (SCH), three compressively-strained InAlGaAs QWs, a 1.5-µm p-InP cladding, and a 100-nm p-InGaAs contact layer. The QWs are designed to have a gain peak at 1540-nm wavelength and a quantum confinement factor of 0.9% per well. For lateral current confinement, a 4-µm-wide and a thin plasma-induced oxide aperture is introduced on top of the p-InGaAs layer, as shown in Fig. 1(c). The chosen oxide thickness is expected to suppress charge tunneling [42]. The silicon waveguide is a rib waveguide with a 230-nm etch depth and a 800-nm width, allowing for single transverse electric (TE) mode around 1.55µm as shown in Fig. 1(d). The chosen top silicon thickness of 500 nm helps achieve active-to-passive-section transmission close to 100% [26]. Regarding the BOX layer thickness, a thinner BOX layer yields lower thermal impedance while causing higher optical leakage. A thickness of 1µm is optimal among commercially available SOI wafer options [26].

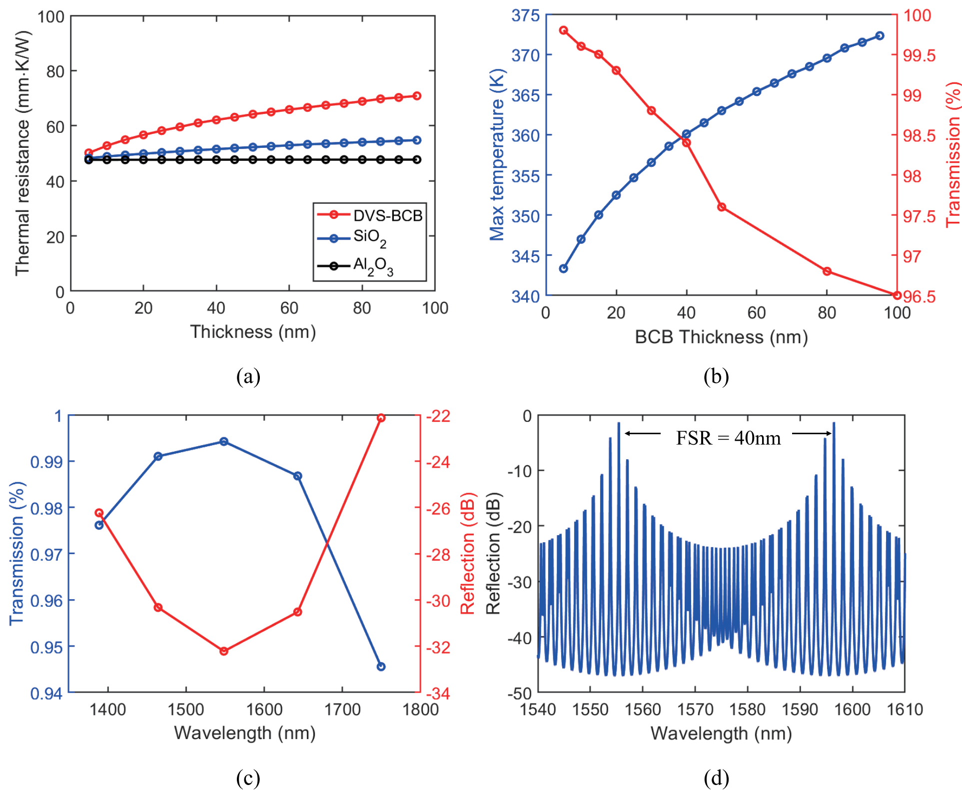

Fig. 2. (a) Simulation of thermal impedance as a function of the thickness of adhesive BCB, SiO_2, and Al_2O_3 layers. (b) Simulated maximum temperature (blue) and passive-to-active section transmission (red) as a function of BCB thickness at a 1550-nm wavelength. (c) Transmission and reflection spectra at the passive-to-active section interface for a 10-nm BCB bonding case. (d) Simulated optical spectral response of the passive cavity in Fig. 1(a2).

The two rings are designed as racetracks combining Euler and circular bends to minimize bending loss [43]. The radii of 60.0µm and 62.5µm are also chosen for minimizing the bending loss as well as giving an FSR of 40 nm. The rings have a gap distance of 400 nm, a coupling length of 14 µm, and a cross-power coupling coefficient of 0.125 with a bus waveguide, which are carefully designed to obtain a Q factor larger than 2×10^4 and a linewidth less than 5 kHz.

The reference laser has a different optical cavity and a gain material from the Vernier laser. It has a single ring of 60-µm radius for the optical cavity. It employs InGaAs QWs instead of

Table 1. Parameters for estimatng thermal impedances and characteristic temperatures

Characteristics	Estimation method	Vernier laser 10-nm BCB InAlGaAs QWs Two rings	Reference laser 40-nm BCB InGaAs QWs One ring
$\partial\lambda/\partial T_{TEC}$ [nm/K]	Experiment (fitting)	0.1176	0.1370
$\partial\lambda/\partial P_a$ [nm/W]	Experiment (fitting)	0.5996	0.9226
Z'_T [K/W]	Experiment	5.099	6.734
Q_{r1}, Q_{r2}	Experiment	2.08×10^4, 1.60×10^4	2.08×10^4, NA
$n_{g,r1}, n_{g,r2}$	Simulation	3.842, 3.854	3.842, NA
L_{r1}, L_{r2} [mm]	Experiment+simulation	1.334, 1.024	1.334, NA
L_p, L_a [mm]	Experiment	8.272, 1.200	7.138, 1.200
$\partial\bar{n}_p/\partial T_p$ [K^{-1}]	Simulation	1.992×10^{-4}	1.992×10^{-4}
$\partial\bar{n}_a/\partial T_a$ [K^{-1}]	Simulation	1.750×10^{-4}	1.750×10^{-4}
Z_T [K/W]	Experiment+simulation	45.09	52.33
$Z_T L_a$ [mm.K/W]	Experiment+simulation	54.10	62.79
T_0, T_r [K]	Experiment (fitting)	64.36, 289.18	55.89, 282.94
T_1 [K], w_a [μm]	Experiment (fitting)	282.0, 20.2	

NA: Not applicable, Red: fitted value

InAlGaAs. The BCB bonding layer thickness is 40 nm. This different configuration is intended to show that the thermal impedance is determined mainly by the downward heat dissipation path, in our case, the BCB layer. We also aimed to demonstrate the robustness of our new method of experimentally estimating the thermal impedance of Vernier laser structures independent of laser cavity structure and gain material type. The characteristic temperature, T_0 is expected to be different from the Vernier laser case, due to different QWs.

Output waveguides are designed to be tilted by 7° with respect to a cleaved facet to suppress back-reflection at the cleaved facet.

2.2. Thermal design with 10 nm BCB bonding

The thermal impedance of the active section in our Vernier laser structure was investigated as a function of the thickness of three bonding interfacial layers, BCB, SiO_2 and Al_2O_3. In the BCB bonding case, it was assumed that a 3-nm Al_2O_3 layer and a 2-nm native oxide layer existed above and below the BCB layer. The simulation was conducted in two dimensions (2D) using COMSOL in which the temperature at the bottom of the SOI wafer was set to 300 K and heat generation density was set to 1.4 W mm^{-1} in the QWs. As shown in Fig. 2(a), the smallest thermal impedance of 47.6 mmK/ W was obtained for the 5-nm Al_2O_3 case, which corresponds to the direct wafer bonding case. The BCB thicknesses of 95 nm, 40 nm, and 10 nm resulted in thermal impedance values of 70.8, 62.1, and 52.7 mmK/ W, which are 48.7%, 30.4% and 10.8% higher than those of the direct bonding case, respectively. A BCB bonding thickness of 100 nm is widely used, while 40 nm is the thinnest reported so far [44].

Figure 2(b) shows the transmission at the passive-to-active section interface and maximum device temperature as a function of BCB thickness. Note that when the BCB thickness is less than 15 nm, the transmission can exceed 99.5%. With 10 nm BCB bonding, a low taper loss of −0.02 dB per taper and a backward reflection of −32 dB can be achieved at a wavelength of 1550 nm, as shown in Fig. 2(c).

Figure 2(d) shows the simulated optical spectrum for the passive Vernier cavity structure, obtained by using Lumerical Interconnect. It predicts that a combination of rings with radii of 60μm and 62.5μm results in an FSR of 40 nm.

3. Thermal impedance analysis for Vernier lasers

In this section, a method for experimentally measuring a thermal impedance of FP laser structures with only an active section is adapted for Vernier laser structures with both active and passive sections.

In general, a laser diode structure consists of an active section of temperature T_a and a passive section of temperature T_p. When the laser is mounted on a thermoelectric cooler (TEC) of temperature, T_{TEC}, the active and passive section temperatures are determined as:

$$T_a = T_{TEC} + \Delta T(P_a) \tag{1a}$$

$$T_p = T_{TEC} \tag{1b}$$

$$P_a = P_{el} - P_{out} \tag{1c}$$

where ΔT is a peak temperature elevation due to Joule heating, P_a. P_{el} and P_{out} are the electrical input power and the optical output power, respectively. At a point 0.4 mm away from the heat source, the temperature elevation drops to 4.7% of the peak value ΔT, as shown in Fig. 3. This implies that the impact of ΔT on T_p can be safely neglected in most of the passive section, considering that the length of the passive section in Vernier lasers is nearly 10 mm. This validates Eq. (1b).

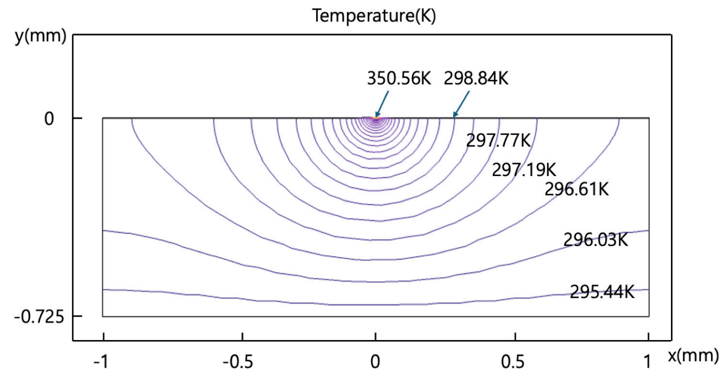

Fig. 3. Steady-state temperature contour around a gain section, simulated using COMSOL. The bottom of the 720-μm-thick SOI substrate is set to a constant temperature of 295.15 K.

Then, the lasing wavelength in vacuum, λ_0 of our Vernier laser cavity is given by the following resonance condition:

$$\frac{2\pi}{\lambda_0}\left[\bar{n}_a(\lambda_0, T_a)L_a + \bar{n}_p(\lambda_0, T_p)L_p\right] = 2\pi m. \tag{2}$$

where $\bar{n}_a$ and $\bar{n}_p$ are modal indices in the active and passive sections, respectively. The lasing wavelength change $\delta\lambda$ due to small variations in refractive indices of the active and passive

Optics EXPRESS

sections, $\delta\bar{n}_{\mathrm{a}}$ and $\delta\bar{n}_{\mathrm{p}}$, is obtained as:

$$\begin{aligned} \delta(2\pi m) &= \delta\left[\frac{2\pi}{\lambda_0}\left(\bar{n}_{\mathrm{a}}L_{\mathrm{a}}+\bar{n}_{\mathrm{p}}L_{\mathrm{p}}\right)\right] \\ 0 &= -\frac{2\pi}{\lambda_0^2}\left(\bar{n}_{\mathrm{a}}L_{\mathrm{a}}+\bar{n}_{\mathrm{p}}L_{\mathrm{p}}\right)\delta\lambda+\frac{2\pi}{\lambda_0}\left(\delta\bar{n}_{\mathrm{a}}L_{\mathrm{a}}+\delta\bar{n}_{\mathrm{p}}L_{\mathrm{p}}\right) \\ \left(\bar{n}_{\mathrm{a}}L_{\mathrm{a}}+\bar{n}_{\mathrm{p}}L_{\mathrm{p}}\right)\delta\lambda &= \lambda_0\left(\delta\bar{n}_{\mathrm{a}}L_{\mathrm{a}}+\delta\bar{n}_{\mathrm{p}}L_{\mathrm{p}}\right) \end{aligned} \tag{3}$$

On the other hand, the thermal impedance of a laser diode structure, Z_{T} is defined in general as,

$$Z_{\mathrm{T}} \equiv \frac{\partial T_{\mathrm{a}}}{\partial P_{\mathrm{a}}} \tag{4}$$

For lasers consisting of only an active section, referred to as FP lasers in this work, the thermal impedance Z_{T} can be approximated as Z'_{T} [26],

$$\begin{aligned} Z'_{\mathrm{T}} &= \left(\left.\frac{\partial\lambda}{\partial P_{\mathrm{a}}}\right|_{T_{\mathrm{TEC}}=\mathrm{const}}\right)\left(\left.\frac{\partial\lambda}{\partial T_{\mathrm{TEC}}}\right|_{P_{\mathrm{a}}=\mathrm{const}}\right)^{-1} \\ &= \frac{\partial T_{\mathrm{TEC}}}{\partial P_{\mathrm{a}}} \approx \frac{\partial T_{\mathrm{a}}}{\partial P_{\mathrm{a}}} = Z_{\mathrm{T}} \end{aligned} \tag{5}$$

Here, Z'_{T} can be experimentally estimated by measuring $(\partial\lambda/\partial P_{\mathrm{a}})$ and $(\partial\lambda/\partial T_{\mathrm{TEC}})$ under conditions of constant TEC temperature and constant heat generation, respectively. The approximate equality in Eq. (5) holds only for FP lasers. It needs to be modified for general laser structures with both active and passive sections, as shown below. The term in the second parenthesis in Eq. (5) can be expressed as,

$$\begin{aligned} \left.\frac{\partial\lambda}{\partial T_{\mathrm{TEC}}}\right|_{P_{\mathrm{a}}=\mathrm{const}} &= \left.\frac{\partial\lambda}{\partial\bar{n}_{\mathrm{a}}}\frac{\partial\bar{n}_{\mathrm{a}}}{\partial T_{\mathrm{a}}}\frac{\partial T_{\mathrm{a}}}{\partial T_{\mathrm{TEC}}}\right|_{P_{\mathrm{a}}=\mathrm{const}} + \left.\frac{\partial\lambda}{\partial\bar{n}_{\mathrm{p}}}\frac{\partial\bar{n}_{\mathrm{p}}}{\partial T_{\mathrm{p}}}\frac{\partial T_{\mathrm{p}}}{\partial T_{\mathrm{TEC}}}\right|_{P_{\mathrm{a}}=\mathrm{const}} \\ &= \frac{\partial\lambda}{\partial\bar{n}_{\mathrm{a}}}\frac{\partial\bar{n}_{\mathrm{a}}}{\partial T_{\mathrm{a}}}\frac{\partial}{\partial T_{\mathrm{TEC}}}\left[T_{\mathrm{TEC}}+\Delta T(P_{\mathrm{a}})\right]_{P_{\mathrm{a}}=\mathrm{const}} + \frac{\partial\lambda}{\partial\bar{n}_{\mathrm{p}}}\frac{\partial\bar{n}_{\mathrm{p}}}{\partial T_{\mathrm{p}}}\frac{\partial}{\partial T_{\mathrm{TEC}}}\left[T_{\mathrm{TEC}}\right]_{P_{\mathrm{a}}=\mathrm{const}} \\ &= \frac{\partial\lambda}{\partial\bar{n}_{\mathrm{a}}}\frac{\partial\bar{n}_{\mathrm{a}}}{\partial T_{\mathrm{a}}} + \frac{\partial\lambda}{\partial\bar{n}_{\mathrm{p}}}\frac{\partial\bar{n}_{\mathrm{p}}}{\partial T_{\mathrm{p}}}, \end{aligned} \tag{6}$$

where Eqs. (1a) and (1b) are substituted into the second equality.

The term in the first parenthesis in Eq. (5) can be expressed as,

$$\begin{aligned} \left.\frac{\partial\lambda}{\partial P_{\mathrm{a}}}\right|_{T_{\mathrm{TEC}}=\mathrm{const}} &= \left.\frac{\partial\lambda}{\partial\bar{n}_{\mathrm{a}}}\frac{\partial\bar{n}_{\mathrm{a}}}{\partial T_{\mathrm{a}}}\frac{\partial T_{\mathrm{a}}}{\partial P_{\mathrm{a}}}\right|_{T_{\mathrm{TEC}}=\mathrm{const}} + \left.\frac{\partial\lambda}{\partial\bar{n}_{\mathrm{p}}}\frac{\partial\bar{n}_{\mathrm{p}}}{\partial T_{\mathrm{p}}}\frac{\partial T_{\mathrm{p}}}{\partial P_{\mathrm{a}}}\right|_{T_{\mathrm{TEC}}=\mathrm{const}} \\ &= \frac{\partial\lambda}{\partial\bar{n}_{\mathrm{a}}}\frac{\partial\bar{n}_{\mathrm{a}}}{\partial T_{\mathrm{a}}}Z_{\mathrm{T}} + \frac{\partial\lambda}{\partial\bar{n}_{\mathrm{p}}}\frac{\partial\bar{n}_{\mathrm{p}}}{\partial T_{\mathrm{p}}}\cdot 0 = \frac{\partial\lambda}{\partial\bar{n}_{\mathrm{a}}}\frac{\partial\bar{n}_{\mathrm{a}}}{\partial T_{\mathrm{a}}}Z_{\mathrm{T}}, \end{aligned} \tag{7}$$

where Eqs. (4) and (1b) are used in the second equality.

Inserting Eqs. (6) and (7) into Eq. (5) gives,

$$Z'_{\mathrm{T}} = \frac{\frac{\partial\lambda}{\partial\bar{n}_{\mathrm{a}}}\frac{\partial\bar{n}_{\mathrm{a}}}{\partial T_{\mathrm{a}}}Z_{\mathrm{T}}}{\frac{\partial\lambda}{\partial\bar{n}_{\mathrm{a}}}\frac{\partial\bar{n}_{\mathrm{a}}}{\partial T_{\mathrm{a}}}+\frac{\partial\lambda}{\partial\bar{n}_{\mathrm{p}}}\frac{\partial\bar{n}_{\mathrm{p}}}{\partial T_{\mathrm{p}}}} = \frac{Z_{\mathrm{T}}}{1+\left(\frac{\partial\lambda}{\partial\bar{n}_{\mathrm{p}}}/\frac{\partial\lambda}{\partial\bar{n}_{\mathrm{a}}}\right)\left(\frac{\partial\bar{n}_{\mathrm{p}}}{\partial T_{\mathrm{p}}}/\frac{\partial\bar{n}_{\mathrm{a}}}{\partial T_{\mathrm{a}}}\right)}.$$

Then, the thermal impedance, Z_{T} and thermal impedance per unit length, $L_{\mathrm{a}}Z_{\mathrm{T}}$ are given as,

$$Z_{\mathrm{T}} = Z'_{\mathrm{T}}\left[1+\left(\frac{\partial\lambda}{\partial\bar{n}_{\mathrm{p}}}/\frac{\partial\lambda}{\partial\bar{n}_{\mathrm{a}}}\right)\left(\frac{\partial\bar{n}_{\mathrm{p}}}{\partial T_{\mathrm{p}}}/\frac{\partial\bar{n}_{\mathrm{a}}}{\partial T_{\mathrm{a}}}\right)\right] = Z'_{\mathrm{T}}\left[1+\frac{L_{\mathrm{p}}}{L_{\mathrm{a}}}\eta_{\mathrm{pa}}\right] \tag{8a}$$

Optics EXPRESS

$$L_a Z_T = Z'_T \left(L_a + L_p \eta_{pa}\right) \tag{8b}$$

where the following relations are used for the second equality. Equations (9a) and (9b) are obtained from Eq. (3):

$$\frac{\partial \lambda}{\partial \bar{n}_a} = \frac{L_a}{\bar{n}_a L_a + \bar{n}_p L_p} \tag{9a}$$

$$\frac{\partial \lambda}{\partial \bar{n}_p} = \frac{L_p}{\bar{n}_a L_a + \bar{n}_p L_p} \tag{9b}$$

$$\eta_{pa} \equiv \left(\frac{\partial \bar{n}_p}{\partial T_p} / \frac{\partial \bar{n}_a}{\partial T_a}\right) \tag{9c}$$

For FP lasers with no passive section ($L_p = 0$), Eq. (8a) is simplified to $Z_T = Z'_T$ in Eq. (5). However, for other lasers like Vernier lasers with both active and passive sections, Eq. (8a) should be used. For Vernier lasers, the passive section length L_p includes the length of straight parts, L_s and the effective lengths of the two rings, $L_{r1,r2}$:

$$L_p = L_s + L_{r1} + L_{r2} = L_s + \frac{Q_1 \lambda_0}{2\pi n_{g,r1}} + \frac{Q_2 \lambda_0}{2\pi n_{g,r2}}, \tag{10}$$

where $Q_{1,2}$ and $n_{g1,g2}$ are the quality factor and group index of the two rings, respectively.

4. Results and discussions

4.1. Fabrication

The Vernier laser and reference laser were fabricated using 10-nm and 40-nm BCB bonding, respectively. In addition, a passive Vernier structure was also fabricated; this structure is identical to the Vernier laser except for the absence of gain material.

For the Vernier laser, 10-nm BCB bonding was successfully conducted as designed, which is the thinnest to our knowledge [22]. Firstly, an SOI die (20 × 20 mm^2) was patterned with silicon rib-waveguides and a III-V epitaxy die (7 × 7 mm^2) was coated with a 3-nm thick Al_2O_3 layer using atomic layer deposition to enhance bonding strength. An adhesion promoter (AP3000) was coated on both SOI and epitaxy dies. Finally, BCB (Cyclotene 3022-35) diluted with mesitylene (ANC Rinse T1100) at a 1:53 ratio was coated only on the III-V die. Then, the SOI and epitaxy dies were bonded and annealed at 230 °C by using a nanoimprint tool (NIL Technology CNI v3.0). After annealing, the InP substrate was removed by wet etching. As shown in Figs. 4(a) and (b), the bonding interface comprises a 2-nm native oxide layer, a 10-nm BCB layer, and a 3-nm Al_2O_3 layer. The bonding interface was uniform: no signs of non-uniformity were observed in the bonded area after substrate removal, as shown in Fig. 4(c). Bonding quality remained intact during subsequent processes including high-temperature steps of SiO_2 deposition at 350 °C (see Fig. 4(d)) and rapid thermal annealing at 420 °C, demonstrating compatibility with post-processing. Although formal reliability testing (e.g., burn-in) was not performed, the device characteristics showed negligible degradation in repeated measurements over several months, indicating the long-term stability of the 10-nm BCB bonding.

After bonding, III-V mesa structures were formed using photo lithography except for a passive-to-active-section mode converter. In forming the mode converter, e-beam lithography was employed since even 0.5μm of misalignment can degrade transmission and reflection performances (see Fig. 5(a)). After forming the III-V mesa, p- and n-metal contacts were formed. In particular, after 4-μm-wide p-contact metal deposition, an oxygen plasma treatment step was intentionally conducted for a few minutes to produce a plasma-induced oxide current aperture on top of the p-doped InGaAs contact layer (see Fig. 1(c)). Photo-BCB planarization was performed to mitigate the step difference due to the mesa structure before forming metal pads. Finally, an 810-nm thick Ti/Cu/Au (10nm/500nm/300nm) metal pad was formed for efficient heat dissipation as well as cost efficiency. Figures 5(a) to (d) show the images of fabricated Vernier laser samples.

Optics EXPRESS

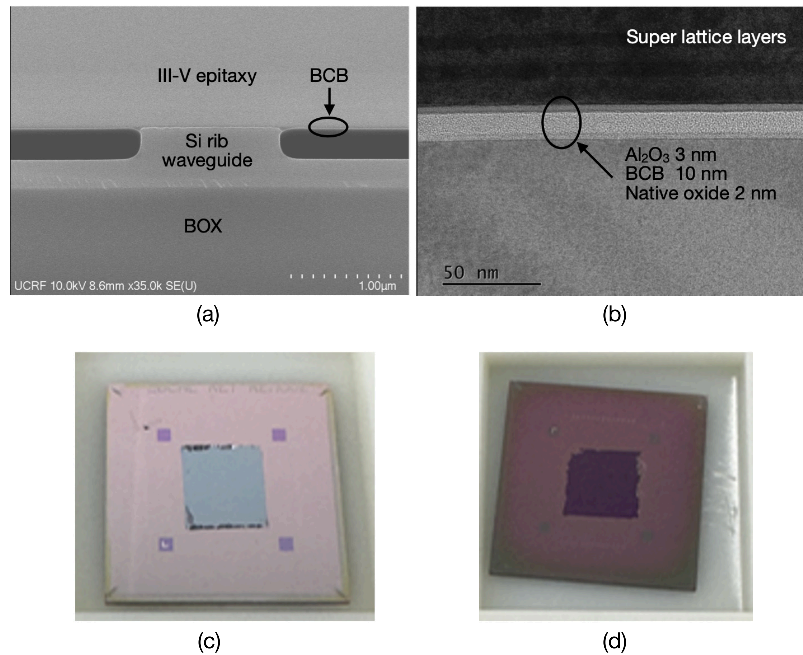

Fig. 4. SEM (a) and TEM (b) images of the 10-nm BCB bonding interface. Optical microscope images of the sample after substrate removal (c) and after SiO_2 deposition at 350 °C (d).

4.2. Characterization results

The I-V curve and output power were measured by using a precision source/measurement unit (Keysight B2902A) and a large-area slim photodetector (Thorlabs S132C). Samples were mounted on a TEC stage to analyze temperature-dependent characteristics. As shown in Fig. 6(a), a single-facet peak power is 6.8 mW from Port 1 of Fig. 1(a1), which is comparable to that of a directly bonded two-ring Vernier laser [16]. The discontinuities in the L-I curve result from longitudinal mode hopping, which can be eliminated by tuning the resonance wavelengths of the two rings. It is noteworthy that no evident thermal roll-over is observed up to 530 mA, which is attributed to the low Z_T value from the 10-nm BCB bonding, as discussed in Section 4.3. The measured threshold current I_{th} of 130 mA and the differential resistance R_d of 2.1 Ω are higher and smaller than expected, respectively. This indicates that the 4-um-wide plasma-induced oxide aperture was not effective, details of which are discussed below in relation to Fig. 7(d).

As shown in Fig. 6(b), the FSR is 40 nm as designed and the SMSR is 46 dB. Using a laser linewidth analyzer (OEWaves OE4000), the linewidth is measured as 2.6 kHz (see Fig. 6(c)), which is similar to the narrowest linewidth value reported for a directly-bonded two-ring Vernier laser [16]. This linewidth corresponds to a coherence length of 47.7 km, which is highly ideal for long-distance coherent LiDAR applications. Figure 6(d) shows a through-port spectrum of the passive Vernier cavity, measured using a tunable laser (Santec TSL-550-A). From the spectrum, the loaded Q-factor values of two rings, Q_1 and Q_2 are measured as 2.08×10^4 and 1.60×10^4, respectively. These values determine ring reflectance values, R_1 and R_2 of 0.7155 and 0.7252 along with ring coupling coefficient, κ^2 of 0.150.

The thermal impedance Z_T values of the Vernier and reference laser samples are estimated by using the revised measurement method explained in Section 3. The change of lasing wavelength with respect to the increases of TEC temperature and active-region heat generation, $\partial\lambda/\partial T_{TEC}$

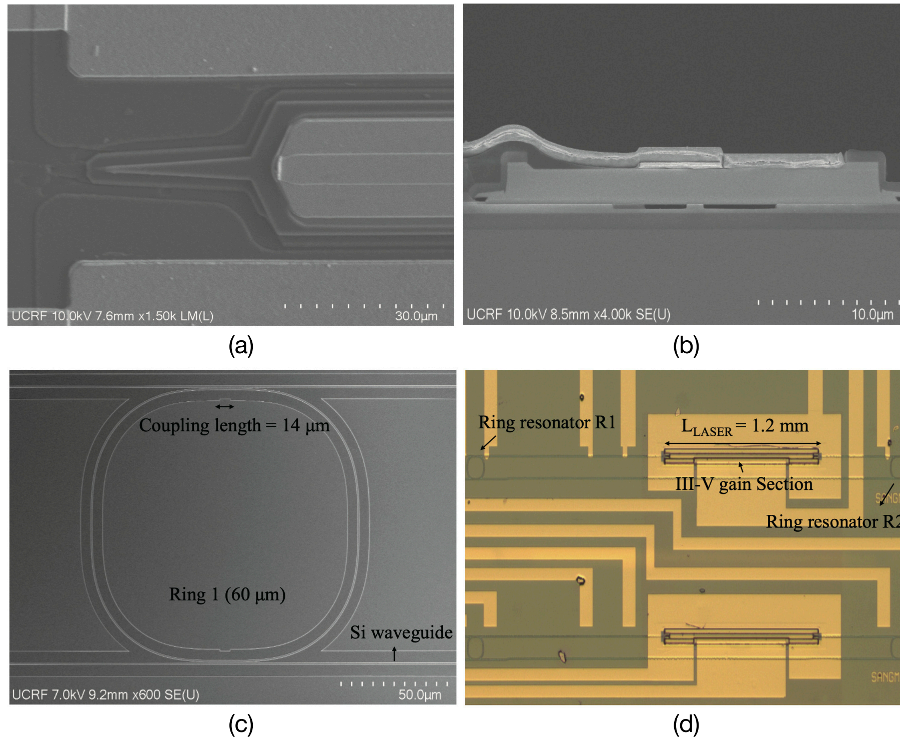

Fig. 5. Images of the fabricated samples: (a) Top-view SEM image of a mode converter from a Si waveguide to a III-V-on-Si waveguide. (b) Cross-sectional SEM image of a III-V-on-Si gain section. (c) Top-view SEM image of a ring resonator. (d) Top-view optical microscope image of an entire Vernier laser.

and $\partial\lambda/\partial P_a$ are measured, as shown in Figs. 7(a) and (b). Then, Z'_T, Z_T, and $Z_T L_a$ values are estimated by using the relations in Eqs. (5), (8a), and (8b), respectively. The temperature dependence of modal indices in η_{pa} of Eq. (9c) is evaluated by using Lumerical MODE. All the obtained and related values are summarized in Table 1. The experimentally estimated $L_a Z_T$ values of the Vernier laser and reference laser structures, 54.10 mmK/W and 62.79 mmK/W differ from the numerically obtained values of 52.75 mmK/ W and 62.10 mmK/ W by 2.6 % and 1.1 %, respectively. This shows that the revised measurement method can precisely estimate the thermal impedance value for various laser structures with various types of passive sections, in our case, one ring in the reference laser and two rings in the Vernier laser.

The characteristic temperatures T_0 of the Vernier and reference lasers are measured as 64.36 K and 55.89 K, respectively, as shown in Fig. 7(c). This reflects that InAlGaAs/InAlGaAs QWs of the Vernier laser are more efficient in suppressing thermal carrier leakage than the InGaAs/InAlGaAs QWs of the reference laser.

Then, a laser model described in Eqs. (11) to (12g) is calibrated with a measured L-I curve of the Vernier laser, as shown in Fig. 7(d). In this calibration, the characteristic temperature for the above-threshold current increment, T_1 [45] and the current aperture width, w_a are used as fitting parameter to be determined to be 282.0 K and 20.2μm, respectively. The plasma-induced-oxide current aperture was formed with a width of 4μm. Considering a lateral diffusion through the 100-nm p-InGaAs and 1500-nm p-InP layers, the active region width, w_a is expected to be 7.2μm(= 4μm + 2 × 1.6μm) at the QW position. The fitted w_a value of 20.2μm indicates that the oxide layer did not effectively prevent the current from tunneling. It could be attributed to

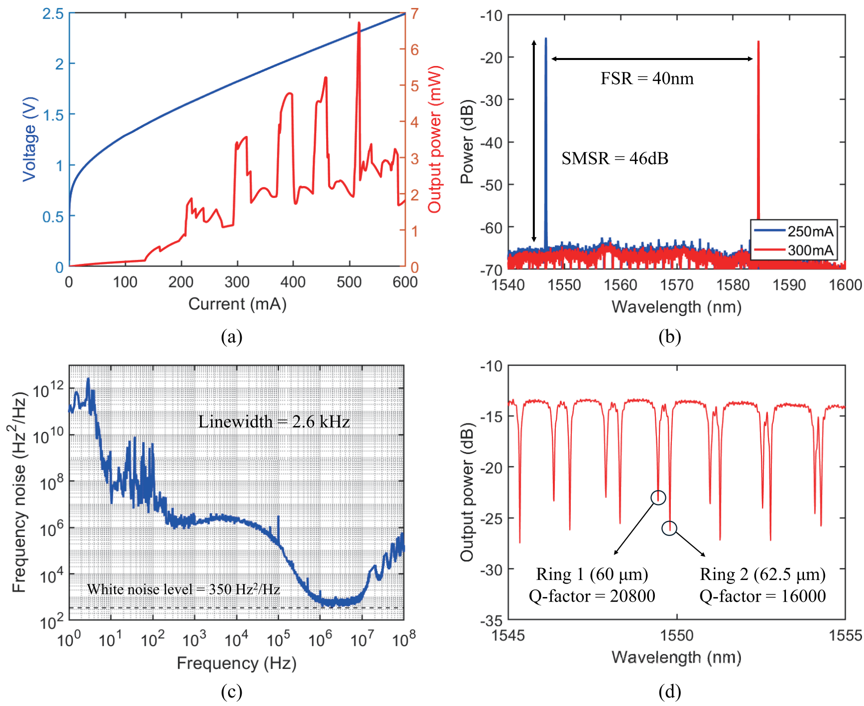

Fig. 6. (a) L-I-V characteristics of the fabricated Vernier laser at T_{TEC} = 13°C. (b) Lasing spectra at 250 mA and 300 mA. (c) Frequency noise spectrum of the Vernier laser. (d) Through-port spectrum of the fabricated passive Vernier cavity sample.

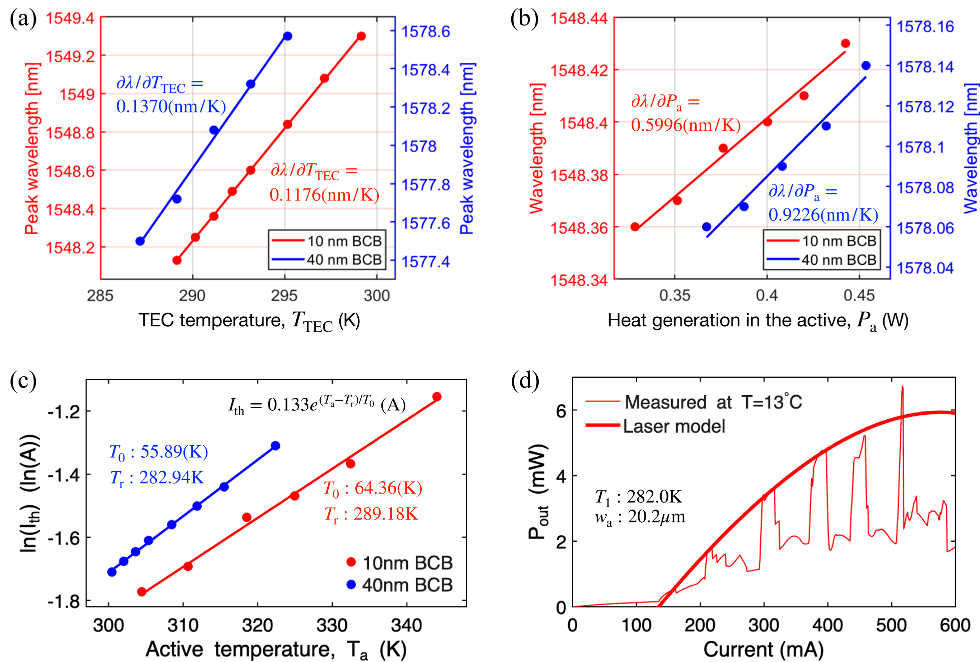

Fig. 7. Lasing wavelength versus (a) TEC temperature T_{TEC} and (b) heat generation in the active section P_a. (c) Threshold current I_{th} on a logarithmic scale versus active region temperature. (d) Calibration of the laser model with the measured L-I curve.

insufficient thickness of the oxide layer and/or conductive In_2O_3, which can be formed after a few minutes of oxygen plasma application to InGaAs and result in current leakage [46–48]. For further analysis, careful investigation on the oxide composition and TEM measurement of the oxide thickness will be required.

Parameters used in the laser model are summarized in Table 2.

$$P_{\text{out}} = \eta_d(I)\frac{hc}{\lambda_0 q}(I - I_{\text{th}}(I)) \tag{11}$$

where

$$\eta_{\text{d}}(I) = \left[\frac{\eta_{\text{i}} F \alpha_{\text{m}}}{\langle\alpha_{\text{i}}\rangle + \alpha_{\text{m}}}\right]_{T=T_{\text{r}}} e^{-(T_{\text{TEC}}+P_{\text{a}}(I)Z_{\text{T}})/T_1} \tag{12a}$$

$$I_{\text{th}}(I) = \left[\frac{q w_{\text{a}} t_{\text{a}} L_{\text{a}}}{\eta_{\text{i}}}\left(AN_{\text{th}} + BN_{\text{th}}^2 + CN_{\text{th}}^3\right)\right]_{T=T_{\text{r}}} e^{(T_{\text{TEC}}+P_{\text{a}}Z_{\text{T}}-T_{\text{r}})/T_0} \tag{12b}$$

$$N_{\text{th}} = e^{g_{\text{th}}/g_{0N}}(N_{\text{tr}} + N_{\text{s}}) - N_{\text{s}} \tag{12c}$$

$$g_{\text{th}} = (\langle\alpha_{\text{i}}\rangle + \alpha_{\text{m}})/(\Gamma_{xy}\Gamma_z) \tag{12d}$$

$$\alpha_{\text{m}} = -\ln(R_1R_2)/(2L_{\text{a}} + 2L_{\text{p}}) \tag{12e}$$

$$\langle\alpha_{\text{i}}\rangle = \langle\alpha_{\text{a}}\rangle_{xy}\Gamma_z + \langle\alpha_{\text{p}}\rangle_{xy}(1-\Gamma_z) \tag{12f}$$

$$P_{\text{a}}(I) = P_{\text{el}} - P_{\text{out}} = I(V_{\text{turn-on}} + IR_{\text{d}}) - P_{\text{out}} \tag{12g}$$

Table 2. Laser model parameters

Parameter	Value	Parmeter	Value	Parameter	Value
T_0	64.36 (K)	L_a	1.2 (mm)	A	1.0×10^7 (s^{-1})
T_r	289.2 (K)	t_a	21 (nm)	B	1.2×10^{-16} (m^3/s)
T_1	282.0 (K)	g_{th}	3.75×10^4 (m^{-1})	C	6.0×10^{-41} (m^6/s)
Z_T (10-nm BCB)	45.09 (K)	α_m	3.46×10^1 (m^{-1})	g_{0N}	3.2×10^5 (m^{-1})
$V_{\text{turn-on}}$	1.1 (V)	R_1, R_2	0.7155, 0.7252	N_s	1.0×10^{24} (m^{-3})
R_d	2.1 (Ω)	$\langle\alpha_i\rangle$	1.0×10^2 (m^{-1})	N_{tr}	1.8×10^{24} (m^{-3})
η_i	0.8	$\langle\alpha_p\rangle_{xy}$	1.2 (dB/cm)	F	0.5
		$\langle\alpha_a\rangle_{xy}$	6.0×10^2 (m^{-1})	Γ_{xy}	0.027
				Γ_z	0.133

4.3. Thermal analysis

To obtain further understanding of the influence of thermal impedance on the laser output, thermal analysis was numerically carried out by using the laser model calibrated in Section 4.2. Six virtual Vernier laser structures with two current apertures w_a of 20.2μm and 4.0μm and three different bonding interfaces of 10-nm BCB, 40-nm BCB, and 5-nm Al_2O_3 (hereafter referred to as directly bonded interface) are compared at T_{TEC} = 13°C and 120 °C. All six structures share identical gain material parameters as listed in Table 2.

As shown in Figs. 8(a) and (b), the 10-nm BCB bonded laser has a considerably higher output power than the 40-nm BCB case for both current aperture cases. In particular, the output power of the 10-nm BCB bonded laser differs by less than 10% from that of the directly bonded laser in most of the practical operating current range, shaded in red in Figs. 8(a) and (b). For the 10-nm BCB bonded laser with w_a of 20.2μm, the thermal rollover starts at 617 mA designated by a red arrow in Fig. 8(a). This is consistent with an experimental observation in Section 4.2, indicating

Optics EXPRESS

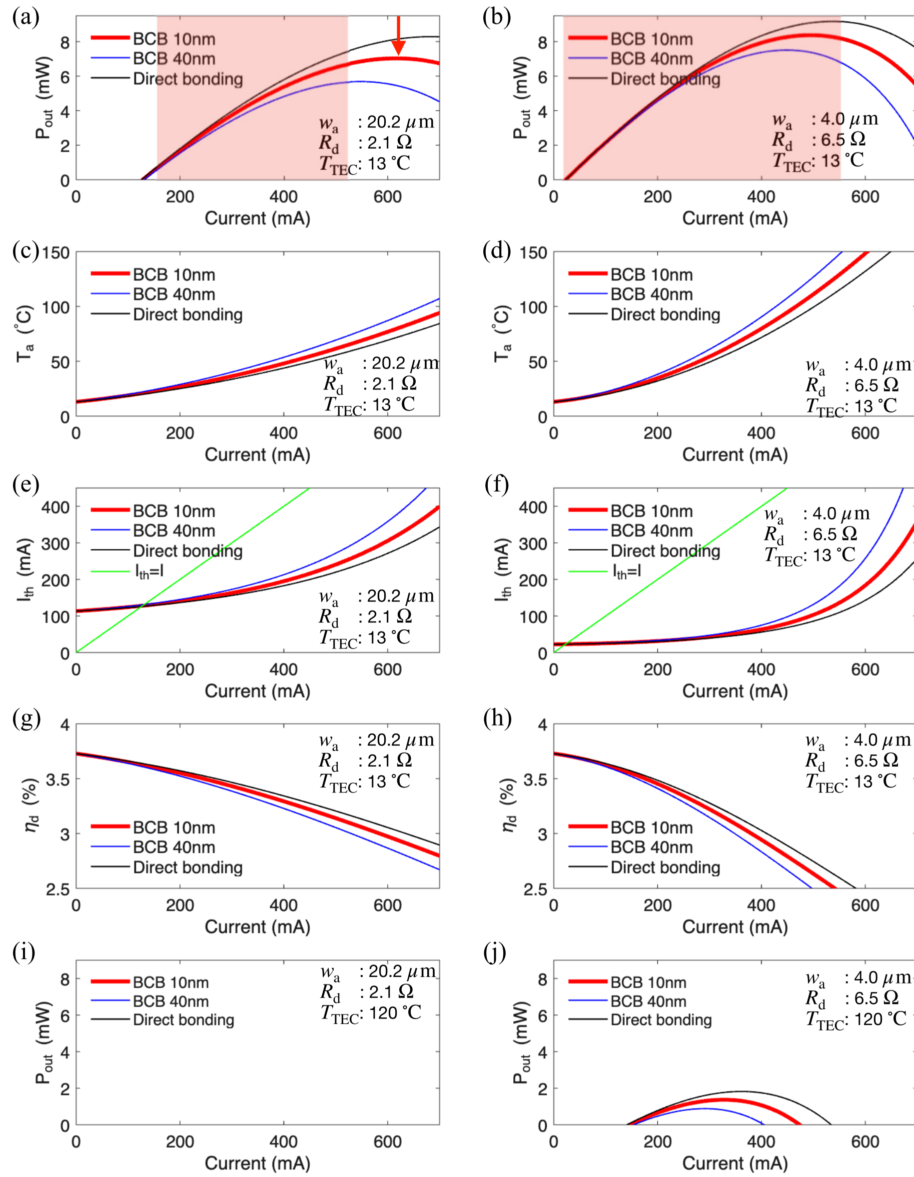

Fig. 8. Numerical thermal analysis results of three Vernier lasers with 10-nm BCB, 40-nm BCB, and directly bonded interfaces for current aperture w_a of 20.2μm (a, c, e, g, i) and 4.0μm (b, d, f, h, j). In (a) and (b), the output power of the 10-nm BCB bonded laser differs by less than 10% from that of the directly bonded laser, in the current range shaded in red color. In (i), all the output powers are negligibly small.

thermal rollover is not evident up to 530 mA. It is also noteworthy that the difference in output power between the BCB bonded and the directly bonded laser structures is smaller for a smaller current aperture w_a of 4.0μm.

The increase in active-region temperature is faster for the 4.0-um aperture laser structures than the 20.2-μm aperture ones, as shown in Figs. 8(c) and (d), since the smaller aperture case has a higher differential resistance R_d of 6.5 Ω, compared to 2.1 Ω of the larger aperture case. However, the increase of threshold current, I_{th} is effectively suppressed for the smaller aperture case, as

Optics EXPRESS

shown in Figs. 8(e) and (f). It is attributed to a very small starting value of 23 mA for the smaller aperture case. The differential quantum efficiency drops faster for the smaller aperture structures, as compared in Figs. 8(g) and (h).

As shown in Figs. 8(i) and (j), at an elevated TEC temperature of 120 °C, the larger aperture laser structures fail to reach the lasing condition, while the smaller aperture lasers emit several mW output power. This implies that having a low threshold current is essential for operation at high ambient temperatures. This numerical test at a high temperature simulates the harsh conditions required for automotive LiDAR applications. The result shows that this type of tunable Vernier lasers can meet conditions for car applications.

In summary, a smaller current aperture provides advantages of a smaller threshold current, a larger differential quantum efficiency and less difference between BCB-bonded and directly bonded lasers, but at the same time, a disadvantage of a larger differential resistance. Overall, the advantages outweigh the mentioned disadvantage for an aperture size of 4μm, allowing for very high-temperature operation.

5. Conclusion

Heterogeneously integrated Si/III-V two-ring Vernier lasers with a 10-nm BCB bonding interface have been demonstrated, which is the thinnest bonding layer reported so far to our knowledge. A two-facet output power of 13.6 mW, a linewidth of 2.6 kHz, a 40-nm FSR and a 46-dB SMSR have been achieved, which are comparable to values reported for a directly bonded Vernier laser. In particular, the similar output power value is attributed to the small thermal impedance value. It is anticipated that a 10-nm BCB bonded Vernier laser with a small aperture such as 4μm will have an output power similar to that of a directly bonded one, up to thermal rollover and is capable of high-temperature operation even at 120 °C. The manufacturability of the Vernier laser with an ultra-thin BCB bonding will be determined by the yield of the BCB bonding, which exceeded 90% in our fabrications of die samples. It is believed that this ultra-thin BCB bonding approach can be an attractive alternative for cases where relaxed requirements for wafer surface flatness are highly desirable.

Funding. Defense Acquisition Program Administration (UI220080TD); National Research Foundation of Korea (NRF-RS-2021-NR060086); Korea Planning and Evaluation of Industrial Technology (RS-2025-02622968).

Acknowledgment. This research was supported by the Challengeable Future Defense Technology Research and Development Program through the Agency for Defense and Development (ADD) funded by the Defense Acquisition Program Administration (DAPA) in 2025 (UI220080TD), by the National Research Foundation of Korea (NRF) grant funded by the Korean government (No. NRF-RS-2021-NR060086), and by the Korea Planning and Evaluation of Industrial Technology (KEIT) grant funded by the Ministry of Trade, Industry and Energy (MOTIE, Korea) (RS-2025-02622968). All device fabrication was performed in our university fab, the Quantum-Nano Fab at UNIST.

Disclosures. The authors declare no conflicting interest.

Data availability. Data underlying the results presented in this paper are not publicly available at this time but may be obtained from the authors upon reasonable request.

References

1. W. Tian, H. He, D. Li, *et al.*, "Progress in research on co-packaged optics," Micromachines **15**(10), 1211 (2024).
2. J. H. Lau, "Co-packaged optics—heterogeneous integration of photonic integrated circuits and electronic integrated circuits," J. Electron. Packag. **147**(1), 011004 (2025).
3. M. Tan and J. Xu, "Co-packaged optics (CPO): status, challenges, and solutions," Front. Optoelectron. **16**(1), 1–176 (2023).
4. B. J. Shastri, A. N. Tait, T. F. de Lima, *et al.*, "Photonics for artificial intelligence and neuromorphic computing," Nat. Photonics **15**(2), 102–114 (2021).
5. P. L. McMahon, "The physics of optical computing," Nat. Rev. Phys. **5**(12), 717–734 (2023).
6. N. Farmakidis, B. Dong, and H. Bhaskaran, "Integrated photonic neuromorphic computing: opportunities and challenges," Nat. Rev. Electr. Eng. **1**(6), 358–373 (2024).
7. C. V. Poulton, M. J. Byrd, P. Russo, *et al.*, "Coherent LiDAR with an 8,192-element optical phased array and driving laser," IEEE J. Sel. Top. Quantum Electron. **28**(5: Lidars and Photonic Radars), 1–8 (2022).

8. Z. Ma, Y. Wan, H. Liang, *et al.*, "Photonic integrated optical phased arrays and their applications [invited]," Chin. Opt. Lett. **22**(2), 020041 (2024).
9. Z. Wu, Y. Song, J. Liu, *et al.*, "Advancements in key parameters of frequency-modulated continuous-wave light detection and ranging: A research review," Appl. Sci. **14**(17), 7810 (2024).
10. J. Lee, D. Shin, B. Jang, *et al.*, "Single-chip beam scanner with integrated light source for real-time light detection and ranging," in *2020 IEEE International Electron Devices Meeting (IEDM)*, (2020), pp. 7.2.1–7.2.4.
11. J. Wang, F. Sciarrino, A. Laing, *et al.*, "Integrated photonic quantum technologies," Nat. Photonics **14**(5), 273–284 (2020).
12. A. W. Elshaari, W. Pernice, K. Srinivasan, *et al.*, "Hybrid integrated quantum photonic circuits," Nat. Photonics **14**(5), 285–298 (2020).
13. L. S. Madsen, F. Laudenbach, M. F. Askarani, *et al.*, "Quantum computational advantage with a programmable photonic processor," Nature **606**(7912), 75–81 (2022).
14. P. Sibson, J. E. Kennard, S. Stanisic, *et al.*, "Integrated silicon photonics for high-speed quantum key distribution," Optica **4**(2), 172–177 (2017).
15. T. Zhou, M. Tang, G. Xiang, *et al.*, "Continuous-wave quantum dot photonic crystal lasers grown on silicon," Nat. Commun. **11**(1), 977 (2020).
16. M. A. Tran, D. Huang, J. Guo, *et al.*, "Ring-resonator based widely-tunable narrow-linewidth Si/InP integrated lasers," IEEE J. Sel. Top. Quantum Electron. **26**(2), 1–14 (2020).
17. G. C. Park, W. Xue, A. Taghizadeh, *et al.*, "Hybrid vertical-cavity laser with lateral emission into a silicon waveguide," Laser Photonics Rev. **9**(3), L11–L15 (2015).
18. E. P. Haglund, S. Kumari, P. Westbergh, *et al.*, "Silicon-integrated short-wavelength hybrid-cavity VCSEL," Opt. Express **23**(26), 33634–33640 (2015).
19. S. Yamaoka, N. P. Diamantopoulos, H. Nishi, *et al.*, "Directly modulated membrane lasers with 108 GHz bandwidth on a high-thermal-conductivity silicon carbide substrate," Nat. Photonics **15**(1), 28–35 (2021).
20. J. Rahimi, J. Van Kerrebrouck, B. Haq, *et al.*, "Demonstration of a high-efficiency short-cavity III–V-on-Si C-band DFB laser diode," IEEE J. Sel. Top. Quantum Electron. **28**(3), 1–6 (2022).
21. D. Huang, D. Huang, Z. Xuan, *et al.*, "A silicon photonic $8\lambda \times 32$ Gb/s/λ WDM transceiver with on-chip DFB laser array, SOA, and CMOS electronics," in *IEEE International Electron Devices Meeting (IEDM)*, (2023).
22. D. Liang and J. E. Bowers, "Recent progress in heterogeneous III-V-on-silicon photonic integration," Light: Adv. Manufact. **2**(1), 59 (2021).
23. S. Keyvaninia, M. Muneeb, S. Stanković, *et al.*, "Ultra-thin DVS-BCB adhesive bonding of III-V wafers, dies and multiple dies to a patterned silicon-on-insulator substrate," Opt. Mater. Express **3**(1), 35–46 (2013).
24. S. Stanković, "Hybrid III-V/Si DFB lasers based on polymer bonding technology," Phd thesis, Ghent University, Faculty of Engineering and Architecture, Department of Information Technology (INTEC), Ghent, Belgium (2013).
25. J. Pu, V. Krishnamurthy, D. K. T. Ng, *et al.*, "Heterogeneous integrated III–V laser on thin SOI with single-stage adiabatic coupler: Device realization and performance analysis," IEEE J. Sel. Top. Quantum Electron. **21**(6), 369–376 (2015).
26. M. N. Sysak, H. Park, A. Fang, *et al.*, "Experimental and theoretical analysis of thermal impedance in a hybrid silicon evanescent laser," in *IEEE Lasers and Electro-Optics Society Annual Meeting Conference Proceedings*, (2007), pp. 827–828.
27. M. Theurer, M. Moehrle, A. Sigmund, *et al.*, "Flip-chip integration of InP to SiN photonic integrated circuits," J. Lightwave Technol. **38**(9), 2630–2636 (2020).
28. A. Marinins, S. Hänsch, H. Sar, *et al.*, "Wafer-scale hybrid integration of InP DFB lasers on Si photonics by flip-chip bonding with sub-300 nm alignment precision," IEEE J. Sel. Top. Quantum Electron. **29**(3), 1–11 (2022).
29. G. Roelkens, J. Zhang, L. Bogaert, *et al.*, "Micro-transfer printing for heterogeneous si photonic integrated circuits," IEEE J. Sel. Top. Quantum Electron. **29**(3: Photon. Elec. Co-Inte. and Ad), 1–14 (2023).
30. S. Chen, W. Li, J. Wu, *et al.*, "Electrically pumped continuous-wave III-V quantum dot lasers on silicon," Nat. Photonics **10**(5), 307–311 (2016).
31. C. Jiang, Y. Kuang, S. Wang, *et al.*, "Demonstration of room-temperature continuous-wave operation of InGaAs/AlGaAs quantum well lasers directly grown on on-axis silicon (001)," Appl. Phys. Lett. **121**(6), 061102 (2022).
32. S. Bao, D. Kim, C. Onwukaeme, *et al.*, "Low-threshold optically pumped lasing in highly strained germanium nanowires," Nat. Commun. **8**(1), 1845 (2017).
33. F. T. A. Pilon, A. Lyasota, Y.-M. Niquet, *et al.*, "Lasing in strained germanium microbridges," Nat. Commun. **10**(1), 2724 (2019).
34. R. W. Martin, J. K. Kozak, K. Anglin, *et al.*, "Optimization of a high-temperature high-pressure direct wafer bonding process for iii-v semiconductors," in *COMSOL Conference*, (2011).
35. E. Kapon and A. Sirbu, "Power-efficient answer," Nat. Photonics **3**(1), 27–29 (2009).
36. A. W. Fang, H. Park, O. Cohen, *et al.*, "Electrically pumped hybrid AlGaInAs-silicon evanescent laser," Opt. Express **14**(20), 9203–9210 (2006).
37. A. W. Fang, H. Park, R. Jones, *et al.*, "Hybrid silicon evanescent devices," Mater. Today **10**(7-8), 28–35 (2007).
38. H. Park, A. W. Fang, S. Kodama, *et al.*, "Hybrid silicon evanescent laser fabricated with a silicon waveguide and III-V offset quantum wells," Opt. Express **13**(23), 9460–9464 (2005).

Optics EXPRESS

39. D. Liang, J. E. Bowers, D. C. Oakley, *et al.*, "High-quality 150 mm InP-to-silicon epitaxial transfer for silicon photonic integrated circuits," Electrochem. Solid-State Lett. **12**(4), H101 (2009).
40. A. A. Khan, T.-K. Nguyen, Q. T. Trinh, *et al.*, "Wafer bonding technologies for microelectromechanical systems and 3d ics: Advances, challenges, and trends," Adv. Eng. Mater. **27**(20), 2500342 (2025).
41. G. Roelkens, B. Batalliou, J. Brouckaert, *et al.*, "Adhesive bonding of iii-v dies to processed soi using bcb for photonic applications," ECS Trans. **3**(6), 321–326 (2006).
42. J. G. Simmons, "Generalized formula for the electric tunnel effect between similar electrodes separated by a thin insulating film," J. Appl. Phys. **34**(6), 1793–1803 (1963).
43. M. Bahadori, M. Nikdast, Q. Cheng, *et al.*, "Universal design of waveguide bends in silicon-on-insulator photonics platform," J. Lightwave Technol. **37**(13), 3044–3054 (2019).
44. K. Van Gasse, R. Wang, and G. Roelkens, "27 dB gain III-V-on-silicon semiconductor optical amplifier with > 17 dBm output power," Opt. Express **27**(1), 293–302 (2019).
45. L. A. Coldren, S. W. Corzine, and M. L. Mashanovitch, *Diode Lasers and Photonic Integrated Circuits* (Wiley, 2019), 3rd ed.
46. Y.-C. Chang, M.-L. Huang, K.-Y. Lee, *et al.*, "Atomic-layer-deposited HfO_2 on $In_{0.53}Ga_{0.47}As$: Passivation and energy-band parameters," Appl. Phys. Lett. **92**(7), 072901 (2008).
47. Y. Lechaux, A. B. Fadjie-Djomkam, S. Bollaert, *et al.*, "Impact of oxygen plasma postoxidation process on Al_2O_3/n-$In_{0.53}Ga_{0.47}As$ metal-oxide-semiconductor capacitors," Appl. Phys. Lett. **109**(13), 131602 (2016).
48. A. S. H. Liao, B. Tell, R. F. Leheny, *et al.*, "Electron transport in $In_{0.53}Ga_{0.47}As$/plasma oxide inversion layers," Appl. Phys. Lett. **44**(3), 344–345 (1984).

114.70.7.203 2026-01-22 03:39:56